Linear Stability Analysis of the Herringbone Groove Journal Bearings in Microsystems: Consideration of Gas Rarefaction Effects

Wang-Long Li[1]
Associate Professor
Institute of Nanotechnology and Microsystems Engineering,
Center for Micro/Nano Science and Technology,
National Cheng Kung University,
No. 1, University Road,
Tainan 701, Taiwan
e-mail: li.dragonpuff@gmail.com
e-mail: dragon@mail.mina.ncku.edu.tw

Rui-Wen Shen
Graduate Student
Department of Mechanical Engineering,
National Kaohsiung University of Applied Sciences,
Kaohsiung 807, Taiwan

The dynamic performance of the herringbone groove journal bearings (HGJBs) with the effects of gas rarefaction taken into account is considered for applications in microsystems. Two important parameters (the Knudsen number Kn and the tangential momentum accommodation coefficients, TMACs or the accommodation coefficients, ACs) that affect gas rarefaction significantly are considered. Small variations in film thickness and pressure from the equilibrium state are substituted into the transient modified molecular gas lubrication (MMGL) equation, which considers effects of gas rarefactions with the Poiseuille and Couette flow rate correctors. The gas film in the rotor-bearing system is modeled as stiffness and damping elements with coefficients dependent on the exciting frequency. The dynamic coefficients are then obtained by solving the linearized MMGL equations. The equations of motion of the rotor as well as the dynamic coefficients are performed for the present linear stability analysis. Due to the exciting frequency-dependent nature of the dynamic coefficients, an iterative method with the golden section technique is introduced in the linear stability analysis of rotor-bearing systems. The critical mass parameters and the related threshold speed are computed and discussed. The results of this study prove that HGJBs in microsystems can operate at concentric conditions at very high speeds.
[DOI: 10.1115/1.3201872]

Keywords: linear stability analysis, MMGL, Knudsen number, tangential momentum accommodation coefficient

1 Introduction

Due to the better dynamic performance and self-sealing characteristics in concentric or nearly concentric operating conditions [1] of herringbone groove journal bearings (HGJBs), they are widely used in rotating disk-spindles and are of potential use in microsystems. The bearing surfaces with grooves are applied to pump the lubricant inward. The use of HGJBs can also generate the radial stiffness at the concentricity of rotors. Plain journal bearings are not operating in concentric conditions due to null radial stiffness. Moreover, the use of gas bearing has the feature in operating in quite lower noise, high speed, and high temperature. They are used to realize better and feasible features as compared with the current conventional ball bearings and oil-lubricated bearings.

In modeling the gas lubrication film in HGJBs, the continuum flow approach with compressible Reynolds equation is utilized as the governing equation. Due to the complexity of herringbone configurations and the gap discontinuity, numerical analysis is needed to solve the compressible Reynolds equation. The finite element method (FEM) [1–3] is a good candidate to treat this configuration with complexity. The effect of groove location and the effect of rotating or stationary herringbone groove on the dynamic characteristics of the bearing system are discussed by solving the compressible Reynolds equation and the equations of motion of the rotor simultaneously in the time domain [2]. On the other hand, the compressible Reynolds equation is linearized by the method of perturbation under the conditions of small variations in film thickness and pressure in the frequency domain [3]. The lubricating gas film is modeled as the dynamic coefficients [4,5] (stiffness and damping coefficients). The dynamic performance of herringbone groove journal bearings is better than that of plain journal bearings, especially at concentric or nearly concentric operating conditions. The pressure distribution in HGJBs comes from the relative motion (rotation) between the bearing and rotor surfaces. The resulting load capacities and dynamic coefficients may induce an eccentric and/or unstable operating state. The linear stability analysis on hydrodynamic gas bearings was first introduced by Lund [4]. The dynamic coefficients were also obtained by using the orbit method [5].

Due to the improvement in manufacturing techniques and the requirement of high speed and low noise characteristics, the size of bearings tends to decrease. In the applications of microsystems, the clearance in bearings decreases further. The continuum modeling (the compressible Reynolds equation) is questionable as the clearance is comparable to the mean free path of gas molecules (which is dependent on the operating conditions such as pressure and temperature, 65 nm at standard ambient temperature and pressure (SATP)) [6–8]. The compressible Reynolds equation should be corrected and extended to consider the effects of gas rarefaction. The developed models include the continuum model as its special case for small Knudsen numbers (an indicator of gas rarefaction, which is defined as the ratio of the mean free path to the characteristic length). Four flow regimes are classified according

[1]Corresponding author.

Contributed by the Tribology Division of ASME for publication in the JOURNAL OF TRIBOLOGY. Manuscript received January 9, 2009; final manuscript received July 14, 2009; published online September 23, 2009. Assoc. Editor: Lyndon S. Stephens. Paper presented at the World Tribology Congress 2009.

to the Knudsen number: the continuum flow ($\mathrm{Kn}<0.01$), the slip flow ($0.01\leq \mathrm{Kn}<0.1$), the transition flow ($0.1\leq \mathrm{Kn}<10$), and the molecular flow ($\mathrm{Kn}\geq 10$). As the Knudsen number is greater than 0.01, the no-slip condition for a fluid on the solid boundary is questionable. The gas-lubricated journal bearings for self-acting gas-lubricated plain journal bearings with slip-flow effects are considered [9]. Later, the modified Reynolds equation with the first-order slip-flow model (the accommodation coefficient (AC) is set to be 0.8) is applied on analyzing the microelectromechanical system (MEMS)-based microrotating machinery [10]. The dynamic coefficients are obtained by solving the linearized modified Reynolds equation in the frequency domain. The same model is also applied to the analysis of air foil bearings in micropower systems [11]. However, the above analyses are restricted to plain journal bearings operating in the slip-flow regime ($0.01\leq \mathrm{Kn}<0.1$).

As the Knudsen number increases further (increases in mean free path or decreases in characteristic length), the flow regime belongs to the transition flow and/or free molecular regime. The MGL equation with Poiseuille flow rate correctors is proposed for an arbitrary Knudsen number [12]. However, this equation is limited for some specific ACs (symmetric molecular interaction, $\alpha_1=\alpha_2=\alpha=0.7$, 0.8, 0.9, and 1.0). To extend the limitation of the MGL equation, databases on Poiseuille and Couette flow correctors [6,7] are obtained numerically as functions of the inverse Knudsen number and asymmetric ACs ($\alpha_1\neq\alpha_2$). Thus, the MMGL equation is proposed, which is valid for an arbitrary Knudsen number and $0.1\leq\alpha\leq 1.0$. The AC, which is a measure of the fraction of air molecules that interact with solid boundaries in a diffusive manner ($\alpha=1$ for diffuse reflections and $\alpha=0$ for specular reflections), has been determined experimentally to be valid between 0.2 and 0.8 [13,14].

In the frequency domain analysis of HGJBs, the dynamic coefficients are always introduced as indicators of the dynamic performance of the system. The dynamic coefficients are dependent on the exciting frequency. Due to this frequency-dependent nature, it takes more time solving the critical mass and critical whirl frequency for further linear stability analysis. The linear stability analysis of foil bearings [15], gas bearings in micro-via drilling spindle system [16], micro-rotor-bearing systems [17], and slot-restricted gas journal bearings [18] is discussed. The slip-flow effects are considered in Ref. [18]. However, the effects of gas rarefaction include two parameters: the Knudsen number and the accommodation coefficients. No article related to linear stability analysis on HGJBs with Kn and AC taken into account was found. The present analysis uses the MMGL equation, which is applicable for arbitrary Knudsen numbers and ACs as the governing equation for HGJBs in microsystems. The dynamic coefficients of the gas film are obtained by solving the linearized MMGL equations. The equations of motion of the rotating part are considered simultaneously to discuss the stability performance. The stability map of the critical (threshold) mass and frequency parameters as functions of bearing numbers and ACs are discussed.

2 Theory

2.1 Governing Equations. The coordinate system, geometry, and orientation of the grooves with respect to the bearing midplane are illustrated in Fig. 1. The grooved journal is the stationary part and the bushing is the rotating part. The dimensionless MMGL equation, which is applicable for arbitrary Knudsen numbers and AC conditions by introducing the Poiseuille [7] and Couette [6] flow rate correctors, in the θ-Z coordinate is expressed as

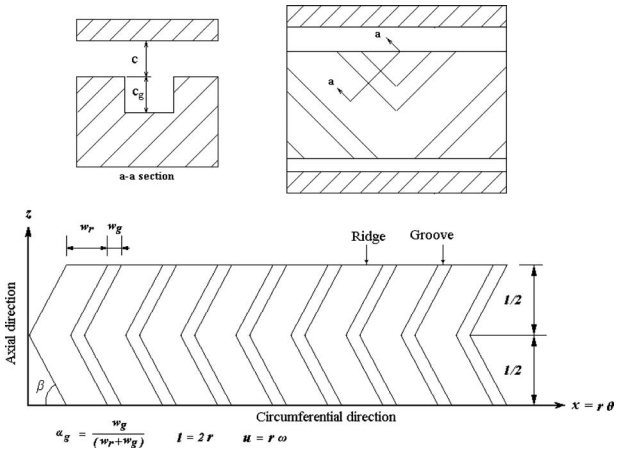

Fig. 1 Geometry of herringbone grooves

$$\frac{\partial}{\partial\theta}\left(PH^3\frac{\partial P}{\partial\theta}Q_p\right)+\frac{\partial}{\partial Z}\left(PH^3\frac{\partial P}{\partial Z}Q_p\right)=\Lambda\frac{\partial(PHQ_c)}{\partial\theta}+\sigma\frac{\partial(PH)}{\partial T} \tag{1}$$

where $H(=h/c)$ is the dimensionless film thickness, $P(=p/p_a)$ is the dimensionless pressure of the gas film, $Q_P(D,\alpha_1,\alpha_2)$ is the Poiseuille flow rate corrector, $Q_C(D,\alpha_1,\alpha_2)$ is the Couette flow rate corrector, $\Lambda=6\mu\omega_r r^2/p_a c^2$ is the bearing number, $\sigma=12\mu\omega_r r^2/p_a c^2=2\Lambda$ is the squeeze number, $D(=D_0PH)$ is the inverse Knudsen number, ω_r is the rotating angular frequency, μ is the viscosity of lubricant, r is the radius of the shaft, c is the concentric clearance, p_a is the ambient pressure, p is the pressure, and h is the film thickness of the lubricating film.

Under dynamic conditions, the dimensionless film thicknesses for well-aligned rotor-bearing systems are expressed as

$$H(\theta,T)\approx H_0+\Delta H=H_0(\theta)+\Delta X(T)\cos\theta+\Delta Y(T)\sin\theta \tag{2}$$

$$H_0(\theta)=1+\eta+\varepsilon_0\cos(\theta-\Phi_0) \tag{3}$$

where $\varepsilon_0=e_0/c$ is the eccentricity ratio and η is the groove depth ($\eta=0$ on the ridge and $\eta=c_g/c$ in the groove).

The pressure variations due to film thickness variation are expressed as

$$P(\theta,Z,T)\approx P_0(\theta,Z)+\Delta P(\theta,Z,T) \tag{4}$$

where $H_0(\theta)$ and $P_0(\theta,Z)$ are the film thickness and pressure distribution operating at steady-state position (e_{x_0},e_{y_0}), respectively.

The flow rate correctors can also be expressed as

$$Q_p=(Q_p)_0+\left(\frac{\partial Q_p}{\partial P}\right)_0\Delta P+\left(\frac{\partial Q_p}{\partial H}\right)_0\Delta H \tag{5}$$

$$Q_c=(Q_c)_0+\left(\frac{\partial Q_c}{\partial P}\right)_0\Delta P+\left(\frac{\partial Q_c}{\partial H}\right)_0\Delta H \tag{6}$$

where $D_0=p_a c/\mu\sqrt{2RT_0}$ and the related derivatives are

$$\left(\frac{\partial Q_p}{\partial P}\right)_0=\left(\frac{\partial Q_p}{\partial D}\right)_0 D_0H_0,\quad \left(\frac{\partial Q_c}{\partial P}\right)_0=\left(\frac{\partial Q_c}{\partial D}\right)_0 D_0H_0$$

$$\left(\frac{\partial Q_p}{\partial H}\right)_0=\left(\frac{\partial Q_p}{\partial D}\right)_0 D_0P_0,\quad \left(\frac{\partial Q_c}{\partial H}\right)_0=\left(\frac{\partial Q_c}{\partial D}\right)_0 D_0P_0 \tag{7}$$

The substitution of the perturbed form in Eqs. (2)–(7) in the MMGL equation (Eq. (1)) results in one steady-state and four first-order equations. The steady (zeroth-order) equation is expressed as

$$\frac{\partial}{\partial\theta}\left[\frac{P_0{H_0}^3}{\sigma}\frac{\partial P_0}{\partial\theta}(Q_p)_0\right]+\frac{\partial}{\partial Z}\left[\frac{P_0{H_0}^3}{\sigma}\frac{\partial P_0}{\partial Z}(Q_p)_0\right]$$
$$=\frac{1}{2}\frac{\partial}{\partial\theta}[P_0H_0(Q_c)_0] \tag{8}$$

and the first-order equation is expressed as

$$\frac{1}{\sigma}\frac{\partial}{\partial\theta}\left\{\frac{\partial P_0}{\partial\theta}P_0{H_0}^3\left[\left(\frac{\partial Q_p}{\partial P}\right)_0\Delta P+\left(\frac{\partial Q_p}{\partial H}\right)_0\Delta H\right]+\frac{\partial P_0}{\partial\theta}(3P_0{H_0}^2\Delta H+{H_0}^3\Delta P)(Q_p)_0+\frac{\partial\Delta P}{\partial\theta}(P_0{H_0}^3)(Q_p)_0\right\}$$
$$+\frac{1}{\sigma}\frac{\partial}{\partial Z}\left\{\frac{\partial P_0}{\partial Z}P_0{H_0}^3\left[\left(\frac{\partial Q_p}{\partial P}\right)_0\Delta P+\left(\frac{\partial Q_p}{\partial H}\right)_0\Delta H\right]+\frac{\partial P_0}{\partial Z}(3P_0{H_0}^2\Delta H+{H_0}^3\Delta P)(Q_p)_0+\frac{\partial\Delta P_0}{\partial Z}(P_0{H_0}^3)(Q_p)_0\right\}$$
$$=\frac{1}{2}\frac{\partial}{\partial\theta}P_0H_0\left[\left(\frac{\partial Q_c}{\partial P}\right)_0\Delta P+\left(\frac{\partial Q_c}{\partial H}\right)_0\Delta H\right]+\frac{1}{2}\frac{\partial}{\partial\theta}(Q_c)_0(P_0\Delta H+H_0\Delta P)+\frac{\partial}{\partial T}(P_0\Delta H+H_0\Delta P) \tag{9}$$

The periodic pressure boundary conditions are used in the circumferential direction. Also, we have the boundary conditions on the two sides ($L=0,1$) as $P_0=1$ and $\Delta P=0$.

Taking the Laplace transformation, the film thickness variation can be expressed as

$$\Delta\bar{H}(\theta,s)=\Delta\bar{X}(s)\cos\theta+\Delta\bar{Y}(s)\sin\theta \tag{10}$$

and the Laplace transformation of pressure variation becomes

$$\Delta\bar{P}(\theta,Z,s)=G_1(\theta,Z,s)\cdot\Delta\bar{X}(s)+G_2(\theta,Z,s)\cdot\Delta\bar{Y}(s) \tag{11}$$

where $G_n(n=x,y)$ are complex functions to be determined and the parameter s is, in general, complex ($s=\beta+j\Omega$, $\beta=0$, $j=\sqrt{-1}$, and $\Omega=\omega/\omega_s$). In the following derivation, $\beta=0$ is used in the determination of the threshold of instability.

The substitution of Eqs. (5)–(7) and Eqs. (10) and (11) in Eq. (9) results in four first-order equations, i.e.,

$$\frac{\partial}{\partial\theta}\left[\frac{P_0{H_0}^3}{\sigma}\frac{\partial G_i}{\partial\theta}(Q_p)_0\right]+\frac{\partial}{\partial Z}\left\{\frac{P_0{H_0}^3}{\sigma}\left[\frac{\partial G_i}{\partial Z}(Q_p)_0\right]\right\}$$
$$=\frac{\partial}{\partial\theta}\left(\frac{P_0H_0}{2}\right)\left[\left(\frac{\partial Q_c}{\partial P}\right)_0G_i+\left(\frac{\partial Q_c}{\partial H}\right)_0c_i\right]+\frac{\partial}{\partial\theta}\frac{(Q_c)_0}{2}(P_0c_i+H_0G_i)-\frac{\partial}{\partial\theta}\left\{\frac{\partial P_0}{\partial\theta}\frac{P_0{H_0}^3}{\sigma}\left[\left(\frac{\partial Q_p}{\partial P}\right)_0G_i+\left(\frac{\partial Q_p}{\partial H}\right)_0c_i+\frac{3}{H_0}c_i+\frac{1}{P_0}G_i(Q_p)_0\right]\right\}$$
$$-\frac{\partial}{\partial Z}\left\{\frac{\partial P_0}{\partial Z}\frac{P_0{H_0}^3}{\sigma}\left[\left(\frac{\partial Q_p}{\partial P}\right)_0G_i+\left(\frac{\partial Q_p}{\partial H}\right)_0c_i+\frac{3}{H_0}c_i+\frac{1}{P_0}G_i(Q_p)_0\right]\right\}+j\Omega\cdot(P_0c_i+H_0G_i) \tag{12}$$

where $c_x=\cos\theta$, $c_y=\sin\theta$, and the boundary conditions are $G_i=0$ at the boundaries.

2.2 Modeling of Gas Film. The load capacities of the gas film could be obtained by integrating the pressure distributions over the bearing surfaces and be expressed as $W=\sqrt{{W_x}^2+{W_y}^2}$, where

$$W_x=\int_0^{l/r}\int_0^{2\pi}(P-1)\cos\theta\ d\theta dZ \tag{13}$$

$$W_y=\int_0^{l/r}\int_0^{2\pi}(P-1)\sin\theta\ d\theta dZ \tag{14}$$

The force of the gas film acting on the rotor surface can be modeled with the dynamic coefficients K_{ij} and D_{ij} ($i=x,y$ and $j=x,y$), i.e.,

$$F_x=-\int\int\Delta P\cos\theta\ dZd\theta=s\cdot D_{xx}\Delta\bar{X}+s\cdot D_{xy}\Delta\bar{Y}+K_{xx}\Delta\bar{X}+K_{xy}\Delta\bar{Y} \tag{15}$$

$$F_y=-\int\int\Delta P\sin\theta\ dZd\theta=s\cdot D_{yx}\Delta\bar{X}+s\cdot D_{yy}\Delta\bar{Y}+K_{yx}\Delta\bar{X}+K_{yy}\Delta\bar{Y} \tag{16}$$

where $M=mc{\omega_r}^2/p_a r^2$, $D_{ij}=d_{ij}c\omega_r/p_a r^2$, $K_{ij}=k_{ij}c/p_a r^2$, $F=f/p_a r^2$, i, $j=x,y$, and $n=x,y$. Therefore, we have the dynamic coefficients as follows:

$$K_{ij}=\text{real part of}\left(-\int\int c_iG_j dZd\theta\right) \tag{17a}$$

and

$$\Omega\cdot D_{ij}=\text{imaginary part of}\left(-\int\int c_iG_j dZd\theta\right) \tag{17b}$$

The rotor-bearing system is modeled with two degrees of freedom, i.e.,

$$M\ddot{X}=-F_x,\quad M\ddot{Y}=-F_y \tag{18}$$

2.3 Linear Stability Analysis. The stability prediction method is mainly from Lund [4]. In order to perform the theoretical analysis of stability, the equations of motion using the dynamic coefficients in the frequency domain are written as

$$\begin{bmatrix}Ms^2+D_{xx}s+K_{xx} & D_{xy}s+K_{xy}\\ D_{yx}s+K_{yx} & Ms^2+D_{yy}s+K_{yy}\end{bmatrix}\begin{Bmatrix}\Delta X_0\\ \Delta Y_0\end{Bmatrix}e^{sT}=0 \tag{19}$$

The determinant has to be zero to satisfy the nontrivial solution, i.e.,

$$\Delta=\begin{vmatrix}Ms^2+D_{xx}s+K_{xx} & D_{xy}s+K_{xy}\\ D_{yx}s+K_{yx} & Ms^2+D_{yy}s+K_{yy}\end{vmatrix}=0 \tag{20}$$

or

$$M^2s^4+(D_{xx}+D_{yy})Ms^3+(K_{xx}+K_{yy}+D_{xx}D_{yy}-D_{xy}D_{yx})Ms^2+(K_{xx}D_{yy}+K_{yy}D_{xx}-K_{xy}D_{yx}-K_{yx}D_{xx})s+(K_{xx}K_{yy}-K_{xy}K_{yx})=0 \tag{21}$$

At the threshold of instability, we can obtain the two equations of the form by introducing $s=0+j\cdot\Omega$ into Eq. (21) and splitting the equation into real and imaginary parts, i.e.,

$$M=\frac{K_{xx}D_{yy}+K_{yy}D_{xx}-K_{xy}D_{yx}-K_{yx}D_{xy}}{\Omega^2(D_{xx}+D_{yy})} \tag{22}$$

$$(K_{xx}-\Omega^2M)(K_{yy}-\Omega^2M)-\Omega^2D_{xx}D_{yy}-K_{xy}K_{yx}+\Omega^2D_{xy}D_{yx}=0 \tag{23}$$

Since the dynamic coefficients are exciting frequency-dependent, the mass and frequency parameters obtained from Eqs. (22) and (23) should be introduced into Eq. (21) to check if all the roots have a nonpositive real part and to check if one of the roots is $s=0+j\cdot\Omega$. The thresholds of instability are then plotted as we obtain the two parameters iteratively under specific operating conditions. As any real part of the four roots in Eq. (21) is positive, the

system is unstable. The stability map can help the designer to have the system operating in the stable region. To judge which region is stable in the stability plot, it is necessary to discuss the effects of mass and frequency parameters on the real part of s.

From the chain rule in calculus, we can introduce the determinant as

$$\Delta \cong \Delta_0 + \left(\frac{\partial \Delta}{i\,\partial \Omega}\right)_0 \cdot ds + \left(\frac{\partial \Delta}{\partial M}\right)_0 \cdot dM \tag{24}$$

At threshold $\Delta=\Delta_0=0$, we have

$$\left(\frac{ds}{dM}\right)_0 = \left(\frac{\partial \beta}{\partial M}\right)_0 + j\left(\frac{\partial \Omega}{\partial M}\right)_0 = \left(\frac{\partial \Delta}{\partial M}\right)_0 / j\left(\frac{\partial \Delta}{\partial \Omega}\right)_0 \tag{25}$$

In addition, we can derive the numerator and denominator as

$$\left(\frac{\partial \Delta}{\partial M}\right)_0 = -\Omega^2(K_{xx}-K_{yy}) + 2\Omega^4 M - j\Omega^3(D_{xx}+D_{yy}) \tag{26}$$

$$\left(\frac{\partial \Delta}{\partial \Omega}\right)_0 = 2[-(K_{xx}K_{yy}-K_{xy}K_{yx}-\Omega^4 M^2) - \Omega \cdot j\Omega^2 M(C_{xx}+C_{yy})] \tag{27}$$

The real part of $(ds/dM)_0$ becomes [19,20]

$$\left(\frac{d\beta}{dM}\right)_0 = \frac{\frac{1}{2}\Omega^4(D_{xx}+D_{yy})\Omega^2(D_{xx}D_{yy}-D_{xy}D_{yx})}{(K_{xx}K_{yy}-K_{xy}K_{yx}-\Omega^4 M^2)^2 + \Omega^2\Omega^4 M^2(D_{xx}+D_{yy})^2} \tag{28}$$

The threshold is obtained from $\beta=0$. On the stability map (e.g., M versus Λ), the two regions split by the threshold line can be judged as stable or unstable by the substitution of the parameters (M and Ω) and by relating K_{ij} and D_{ij} into Eq. (28). If $(d\beta/dM)_0<0$, it means as M increases, the system becomes stable. Otherwise, the system becomes unstable as M increases.

3 Results and Discussion

Following the solver developed in Ref. [21], the partial differential equations (PDEs) (Eqs. (8) and (12)) of the present problems are solved by FEM mapped quad mesh that consists of 800 elements and 16,905 degrees of freedom. The grid density is doubled to check for the precision requirement. The convergence for relative errors within 10^{-5} is achieved for each grid. The comparison of dimensionless load capacities, attitude angles, and stiffness coefficients with those by Faria [3] is proposed in our previous paper in Ref. [21]. Good agreement between the numerical scheme and Faria [3] are found, as all the relative errors are smaller than 0.1%.

It is hard to find the stability map of HGJBs to compare with. Most of the papers treat the dynamic coefficients as excitation frequency-independent, even though they are excitation frequency-dependent. To validate the correctness of the present stability map, the stability analysis of foil bearings by Vleugels et al. [15] without bearing compliance is compared with the present results. The plain journal cases are analyzed by setting the groove depth=0 ($c_g=0$) and flow rate correctors=1 ($Q_P=Q_C=1$) in the present simulation. However, the "cavitation" type boundary conditions in Ref. [15] were used for the nonfixed top foil. The dimensionless critical mass parameters are plotted as functions of bearing numbers at low eccentricity ratio ($\varepsilon=0.3$), as shown in Fig. 2(*a*). The comparison seems marginally acceptable. The discrepancy comes from the boundary setting (cavitation boundary) in foil bearings [15]. As the top foil is, in general, not fixed to the flexible element, it could lose contact with the flexible element when a subambient pressure is reached. The Reynolds cavitation boundary conditions [15] ($P=1$, $\partial P/\partial\theta=0$ at $\theta=\theta_b$) were used at the part of the foil to avoid subambient pressure. In addition, the dimensionless load capacities and stiffness coefficients are also

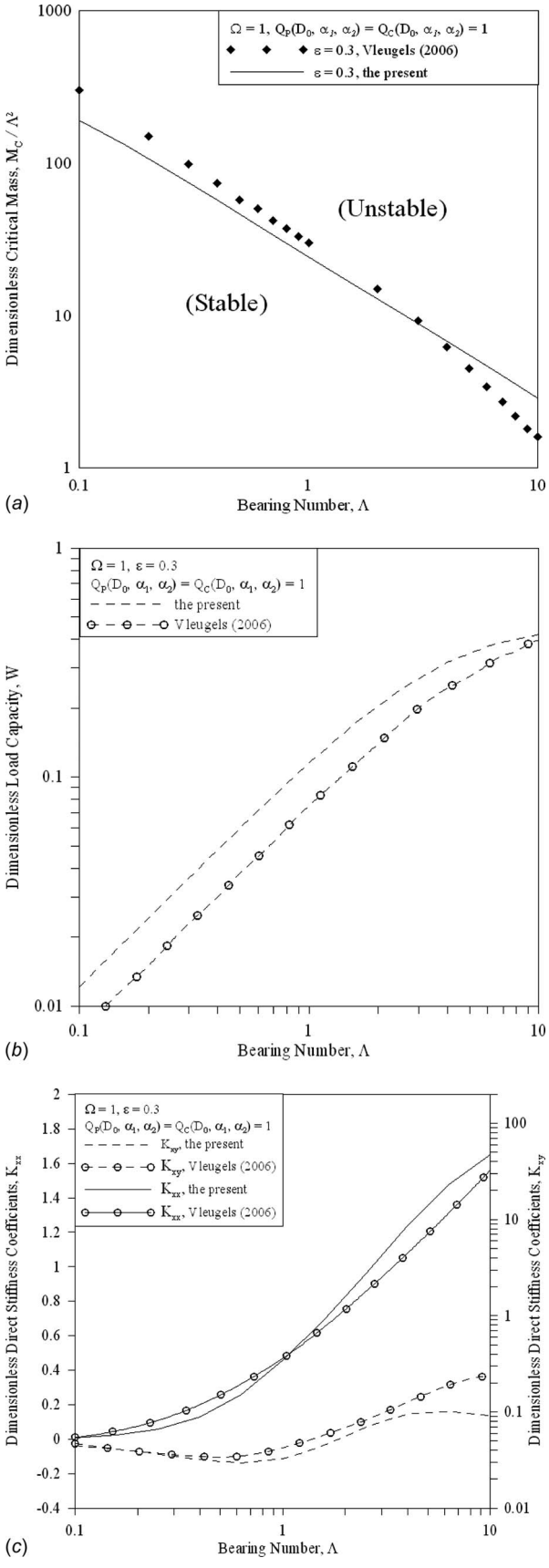

Fig. 2 (*a*) Comparison of dimensionless critical mass parameters with those by Vleugels et al. [15], (*b*) comparison of dimensionless load capacities with those by Vleugels et al. [15], and (*c*) comparison of dimensionless stiffness coefficients with those by Vleugels et al. [15]

Table 1 Basic geometric parameters of HGJBs

l	Length of the bearing	2×10^{-4} m
r	Radius of the rotor	1×10^{-4} m
c	Clearance of the bearing	2×10^{-7} m
c_g	Groove depth	2×10^{-7} m
μ	Gas viscosity	1.8×10^{-5} Pa s
β	Groove angle	30 deg
N_g	Groove number	8
α_g	Groove width ratio	0.25
ε	Eccentricity ratio	0
p_a	Ambient pressure	0.101 MPa

compared, as shown Figs. 2(*b*) and 2(*c*), respectively. We find some discrepancies in the dimensionless load capacities and direct stiffness coefficients. The discrepancy for the dimensionless critical mass parameter comes from the discrepancy of cross stiffness coefficients and dimensionless load capacities. Most of the discrepancy comes from the setting of cavitation boundary conditions in Ref. [15].

3.1 Effects of Eccentricity Ratios. Understanding the effects of groove geometry and operating conditions on HGJBs is important on the design of HGJB systems. The geometry and operation conditions for the present analysis are listed in Table 1. The data shown in Table 1 is for simulation purpose. The present research mainly focuses on studying the effects of Kn and AC on the stability performance of a rotor-bearing system and on solving the problem of frequency-dependent dynamic coefficients (stiffness and damping) of the gas film in the equations of motion. Although the present data in Table 1 are hard to realize in today's manufacturing technology, it is but helpful to discuss the gas rarefaction effects (Kn and AC) on the system by solving the modified Reynolds equation. In addition, the molecular mean free path increases as the temperature increases. Thus, the gas rarefaction effects become especially significant as the operation temperature increases [10]. Therefore, the gas rarefaction is of importance even in the present manufacturing technology. The present model is of potential use as the manufacturing technology improved further.

As shown in Fig. 3, the critical mass parameters (M_C) and related frequencies (Ω) are plotted as functions of bearing numbers for various eccentricity ratios at the groove depth ratio (η

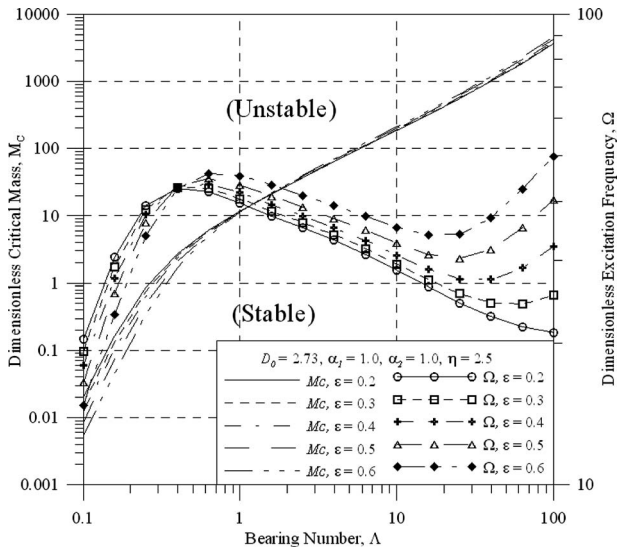

Fig. 3 Stability map plotted as functions of bearing numbers for various eccentricity ratios

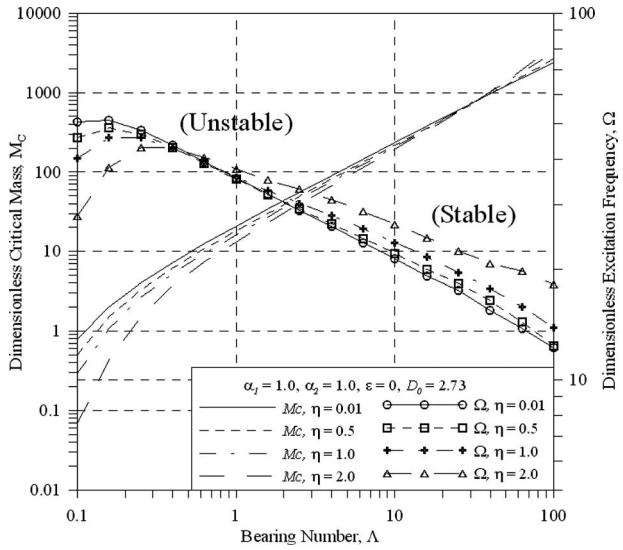

Fig. 4 Stability map plotted as functions of bearing numbers for various groove depth ratios

$=c_g/c=2.5$). In the region of bearing number $\Lambda<1$, the effects of the eccentricity ratio are significant. The critical mass parameter increases as the eccentricity ratio decreases. In the region of bearing number $\Lambda>1$, the effects of eccentricity on the critical mass parameters almost diminish. The critical mass parameter increases as the bearing number increases. Even the eccentricity ratio affects the critical mass parameters slightly. We have a higher critical mass parameter operating at a higher eccentricity ratio; or we can state that the system is more stable for operating conditions at a low eccentricity ratio with a low bearing number ($\Lambda<1$), or at a high eccentricity ratio with a higher bearing number ($\Lambda>1$). The change in the eccentricity ratio also affects the minimum film thickness, and thus the inverse Knudsen number ($D_{\min}=D_0PH_{\min}$) at minimum film thickness $H_{\min}=1-\varepsilon$. The bearing number is defined at the nominal clearance (c). Also, we have larger threshold frequencies for lower eccentricity ratios at bearing numbers around $\Lambda<0.4$. We have lower threshold frequencies for lower eccentricity ratios at bearing numbers around $\Lambda>0.4$. The reverse point for a critical mass parameter and a threshold frequency is around $\Lambda=1$ and 0.4, respectively.

3.2 Effects of Groove Depth Ratios. To discuss the effects of the groove depth ratio ($\eta=c_g/c$) on the stability map, the dimensionless critical mass parameters and threshold frequencies are plotted as functions of bearing numbers for various η at concentric conditions ($\varepsilon=0$). The results in Fig. 4 show that the system is more stable for a lower groove depth ratio at the region of bearing number $\Lambda<30$. At the region of bearing number $\Lambda>30$, the system is slightly stable for a higher groove depth ratio as compared with those for a low groove depth ratio. The reverse point for a critical mass parameter and related threshold frequency occurs around $\Lambda=30$ and 0.4, respectively.

3.3 Effects of Groove Number. In Fig. 5, the effects of the groove number on the stability map are plotted. It seems that the groove numbers are of little effect on the stability map except for the threshold frequency at high bearing numbers. Although the groove number affects the load capacities, it has a little effect on the critical mass in the stability map at concentric operating conditions.

3.4 Effects of Gas Rarefactions. Two parameters, the Knudsen number (Kn) and the accommodation coefficients (α_1,α_2), are used to reflect the effects of gas rarefaction on the stability map.

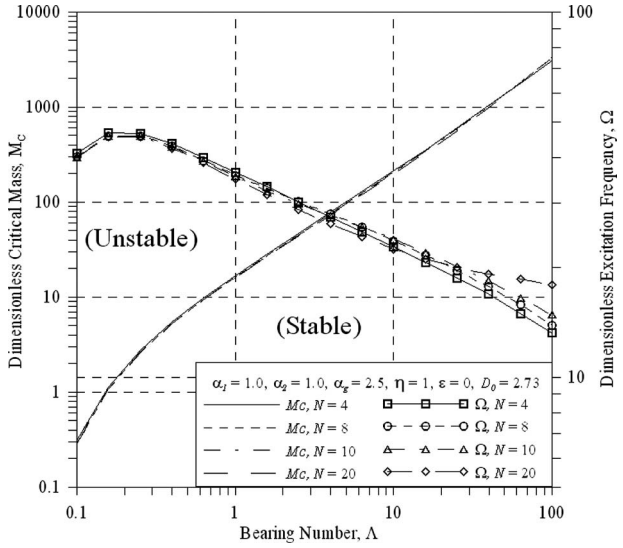

Fig. 5 Stability map plotted as functions of bearing numbers for various groove numbers

They are important indicators of gas rarefaction. The effects of gas rarefaction increase as the AC decreases or Kn increases. As shown in Figs. 6(*a*)–6(*c*), the stability maps are plotted as functions of inverse Knudsen numbers ($D_0 = \sqrt{\pi h}/2\lambda = \sqrt{\pi}/2\mathrm{Kn}_0$) for various groove depth ratios at bearing numbers $\Lambda = 1$, 10, and 100, respectively. We can see that the critical mass parameter and the related threshold frequency increase asymptotically as D_0 increases. As D_0 increases further, the gas rarefaction decreases. The continuum flow modeling is more feasible in that region. The reverse point of D_0 at which the values of threshold frequencies reverses for various groove depth ratios decreases as the bearing number increases. Moreover, the reverse point of D_0 at which the values of critical mass parameters reverses for various groove depth ratios decreases as the bearing number increases. The results in Figs. 6(*a*) and 6(*b*) show that the system is more stable for a smaller groove depth ratio or a larger D_0. A larger D_0 means more continuum flow. The critical mass parameter increases asymptotically to a constant as D_0 increases further to the continuum flow region. At bearing number $\Lambda = 10$, we can find a similar trend as compared with that at $\Lambda = 1$. However, different trends are found in Fig. 6(*c*) at $\Lambda = 100$. The system is more stable for a low groove depth ratio at a lower D_0. Moreover, the system is more stable for a high groove depth ratio at a higher D_0.

To discuss the effects of ACs on the stability map, the dimensionless critical mass parameters are plotted as functions of ACs for various combinations of ACs, as shown in Figs. 7(*a*)–7(*c*), for $\Lambda = 1$, 10, and 100, respectively. In the combinations of α_1, α_2, surface 1 is rotating and surface 2 is stationary. From the Poiseuille flow rate corrector $Q_P(D, \alpha_1, \alpha_2)$, we have the symmetric properties, i.e., $Q_P(D, \alpha_1, \alpha_2) = Q_P(D, \alpha_2, \alpha_1)$. From the Couette flow rate corrector $Q_C(D, \alpha_1, \alpha_2)$, we have the asymmetric properties $Q_C(D, \alpha_1, \alpha_2) + Q_C(D, \alpha_2, \alpha_1) = 2$. The AC on the sliding surface (surface 1, α_1) affects the load capacity more significantly as compared with the AC on the stationary surface (α_2) [21] does. From Figs. 7(*a*)–7(*c*), the critical mass parameter increases as gas rarefaction effects decrease. That is, the stability region increases as gas rarefaction decreases (α or D_0 increases). As the flow is more continuum (gas rarefaction effects decreases), the stability region increases. It is necessary to include the effects of gas rarefaction in the analysis of microsystems. For low bearing cases ($\Lambda = 1$), as shown in Fig. 7(*a*), the critical mass parameter obtained from the combinations of α_1, α_2 is almost the same as that from α_2, α_1. As the bearing number increases, the critical mass param-

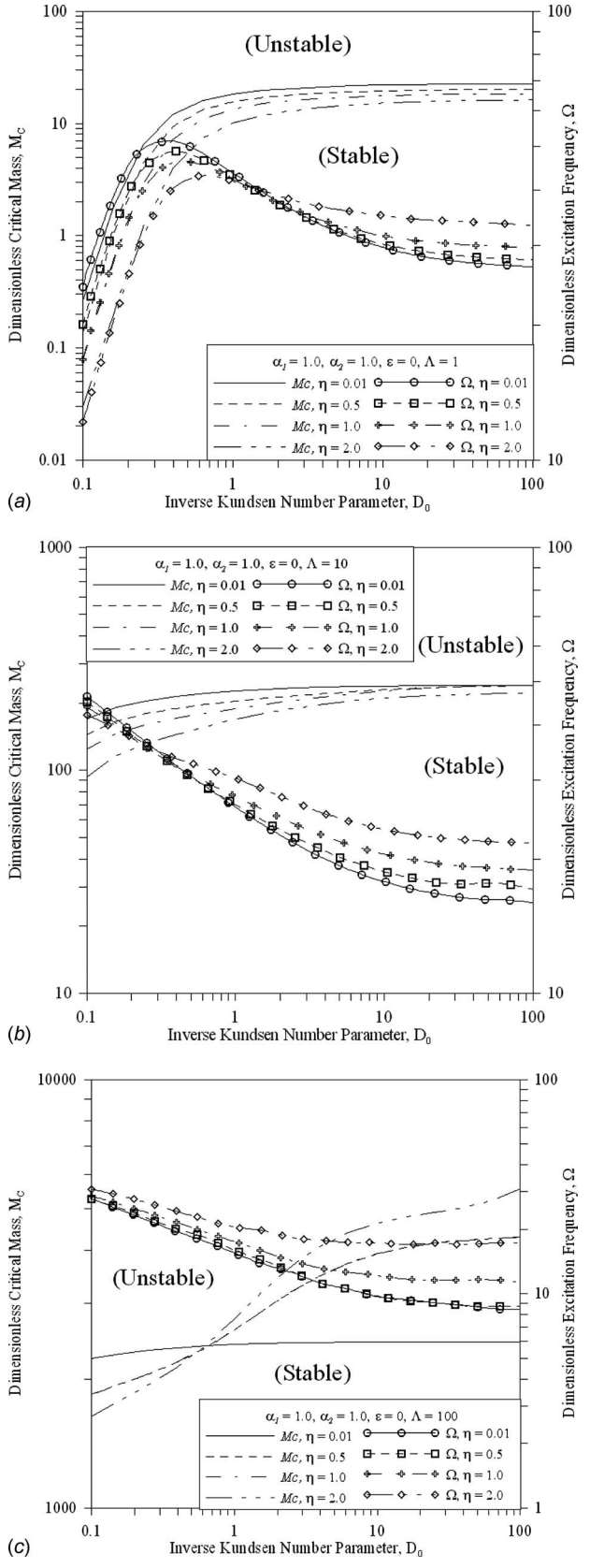

Fig. 6 (*a*) Stability map plotted as functions of inverse Knudsen numbers for various eccentricity ratios for $\Lambda = 1.0$, (*b*) stability map plotted as functions of inverse Knudsen numbers for various eccentricity ratios for $\Lambda = 10$, and (*c*) stability map plotted as functions of inverse Knudsen numbers for various eccentricity ratios for $\Lambda = 100$

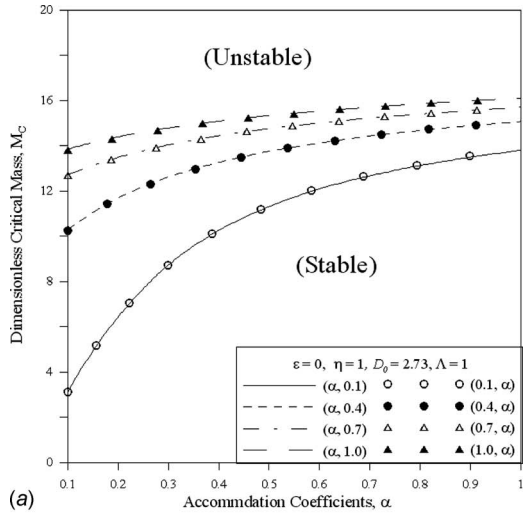

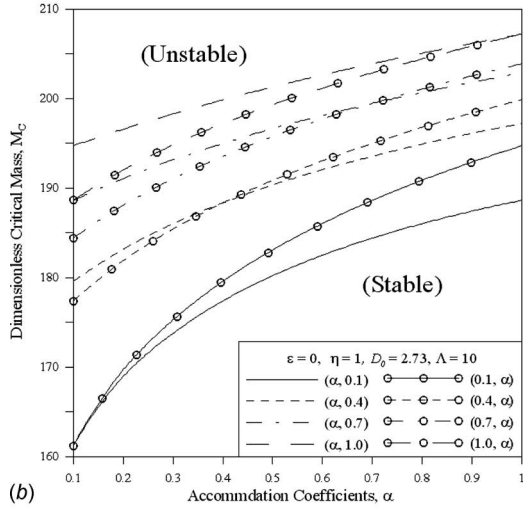

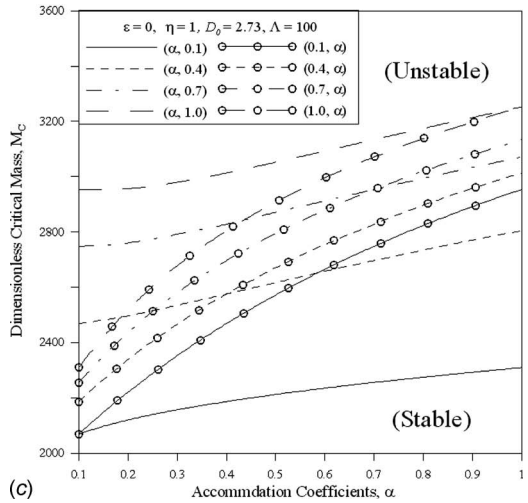

Fig. 7 (*a*) Stability map plotted as functions of ACs for various combinations of ACs at Λ=1.0, (*b*) stability map plotted as functions of ACs for various combinations of ACs at Λ=10, and (*c*) stability map plotted as functions of ACs for various combinations of ACs at Λ=100

eters increase further. The AC on the sliding surface affects the critical mass parameter significantly as the bearing number increases, i.e., $M_C(\alpha,1) > M_C(1,\alpha)$.

4 Conclusion

The linear stability analysis of herringbone groove journal bearings is proposed by solving the linearized MMGL equation and the equations of motion of the rotor. The frequency-dependent nature of the dynamic coefficients makes it difficult to solve for the linear stability analysis of the system. The effects of groove depth ratios, groove numbers, bearing numbers, and gas rarefactions (inverse Knudsen numbers and ACs) on the stability maps are discussed. Some important results are listed below.

(1) The grooved journal bearing has better stability performance to operate at concentric conditions as compared with plain journal bearings.
(2) The stability region (critical mass parameter) is larger for smaller eccentricity ratios at low bearing numbers ($\Lambda < 1$), and is slightly larger for larger eccentricity ratios at high bearing numbers ($\Lambda > 1$).
(3) The stability region is larger for smaller groove depth ratios at low bearing numbers ($\Lambda < 30$), and is slightly larger for larger groove depth ratios at high bearing numbers ($\Lambda > 30$).
(4) The groove numbers affect the critical mass parameters slightly.
(5) The stability region increases as the effects of gas rarefaction decrease (lower D_0 or smaller ACs).
(6) The AC on the sliding surface affect the stability more significantly as compared with the AC on the stationary surface does.

Acknowledgment

The present research was supported by the NSC, Taiwan (Contract No. NSC 96-2221-E-006-337).

Nomenclature

c = concentric clearance (m)
c_g = groove depth (m)
e = eccentricity (m)
e_{x0}, e_{y0} = eccentricities at steady-state (m)
D = inverse Knudsen number ($=D_0PH$)
D_0 = reference inverse Knudsen number
d_{ij} = damping coefficient of gas film ($i=x,y$) (N m/rad)
D_{ij} = dimensionless damping coefficient of gas film ($=d_{ij}c\omega/p_ar^2$; $i=x,y$ and $j=x,y$)
G_n = complex functions ($n=x,y$)
h = film thickness of lubricating film (m)
H = dimensionless film thickness ($=h/c$)
H_0 = dimensionless film thickness at steady-state position
ΔH = dimensionless film thickness variation
k_{ij} = stiffness coefficient of gas film ($i=x,y$ and $j=x,y$) (N m/rad)
K_{ij} = dimensionless stiffness coefficient of gas film ($=k_{ij}c/p_ar^2$; $i=x,y$ and $j=x,y$)
m = mass of the rotor (kg)
M = dimensionless mass parameter
M_C = dimensionless critical mass parameter
p = pressure distribution of the gas film
P = dimensionless pressure in the gas film ($=p/p_a$)
P_0 = dimensionless pressure in the gas film at steady-state position
p_a = ambient pressure (N/m^2)
ΔP = dimensionless pressure variation
r = radius of the rotor (m)
t = time variable
T = the dimensionless time ($=\omega_r t$)

w = load capacity (N)
W = dimensionless load capacity ($=w/p_a r^2$)
$\Delta\bar{X}$ = perturbed dimensionless displacements in the x-direction
$\Delta\bar{Y}$ = perturbed dimensionless displacements in the y-direction
X, Y, Z = rectangular coordinates
α_i = tangential momentum accommodation coefficient of the ith surface ($i=1,2$)
β = real part of s
ε = eccentricity ratio
ω_r = rotor angular velocity (rad/s)
θ = coordinate initiate from the negative x-axis (rad)
σ = squeeze number ($=12\mu\omega_r r^2/p_a c^2$)
μ = viscosity of gas (Pa s)
η = groove depth ($\eta=0$ on the ridge and $\eta=c_g/c$ in the groove)
λ = mean free path of molecules
Λ = bearing number ($=6\mu\omega_r r^2/p_a c^2$)
Φ_0 = attitude angle at steady-state
Ω = dimensionless exciting frequency

References

[1] Bonneau, D., and Absi, J., 1994, "Analysis of Aerodynamic Journal Bearings With Small Number of Herringbone Grooves by Finite Element Method," ASME J. Tribol., **116**, pp. 698–704.
[2] Jang, G. H., and Yoon, J. W., 2002, "Nonlinear Dynamic Analysis of a Hydrodynamic Journal Bearing Considering the Effect of Rotating or Stationary Herringbone Groove," ASME J. Tribol., **124**, pp. 297–304.
[3] Faria, M. T. C., 2001, "Some Performance Characteristics of High Speed Gas Lubricated Herringbone Groove Journal Bearings," JSME Int. J., Ser. C, **44**(3), pp. 775–781.
[4] Lund, J. W., 1968, "Calculation of Stiffness and Damping Properties of Gas Bearings," ASME J. Lubr. Technol., **90**, pp. 793–803.
[5] Czolczynski, K., 1996, "How to Obtain Stiffness and Damping Coefficients of Gas Bearings," Wear, **201**, pp. 265–275.
[6] Li, W.-L., 2002, "A Database for Couette Flow Rate—Consideration of the Effects of Non-Symmetric Molecular Interactions," Trans. ASME, J. Tribol., **124**, pp. 869–873.
[7] Li, W.-L., 2003, "A Database for Interpolation of Poiseuille Flow Rate for Arbitrary Knudsen Number Lubrication Problems," J. Chin. Inst. Eng., **26**(4), pp. 455–466.
[8] Kim, D., Lee, S., Bryant, M. D., and Ling, F. F., 2004, "Hydrodynamic Performance of Gas Microbearings," ASME J. Tribol., **126**, pp. 711–718.
[9] Malik, M., 1984, "Theoretical Considerations of Molecular Mean Free Path Influenced Slip in Self-Acting Gas-Lubricated Plain Journal Bearings," Journal of Mechanical Science, **198C**, pp. 25–31.
[10] Lee, Y.-B., Kwak, H.-D., Kim, C.-H., and Lee, N.-S., 2005, "Numerical Prediction of Slip Flow Effect on Gas-Lubricated Journal Bearings for MEMS/MST-Based Micro-Rotating Machinery," Tribol. Int., **38**, pp. 89–96.
[11] Lee, Y.-B., Park, D.-J., Kim, C.-H., and Ryu, K., 2007, "Rotordynamic Characteristics of a Micro Turbo Generator Supported by Air Foil Bearings," J. Micromech. Microeng., **17**, pp. 297–303.
[12] Fukui, S., and Kaneko, R., 1990, "A Database for Interpolation of Poiseuille Flow Rates for High Knudsen Number Lubrication Problems," ASME J. Tribol., **112**, pp. 78–83.
[13] Lord, R. G., 1976, "Tangential Momentum Accommodation Coefficients of Rare Gases on Polycrystalline Metal Surfaces," *Rarefied Gas Dynamics*, Tenth Symposium, New York, pp. 531–538.
[14] Arklic, E. B., 1997, "Measurement of the Mass Flow and Tangential Momentum Accommodation Coefficient in Silicon Micromachined Channels," Ph.D. thesis, Massachusetts Institute of Technology, Cambridge, MA.
[15] Vleugels, P., Waumans, T., Peirs, J., Al-Bender, F., and Reynaerts, D., 2006, "High-Speed Bearings for Micro Gas Turbines: Stability Analysis of Foil Bearings," J. Micromech. Microeng., **16**, pp. S282–S289.
[16] Huang, B. W., and Kung, H. K., 2003, "Variations of Instability in a Rotating Spindle System With Various Bearings," Int. J. Mech. Sci., **45**, pp. 57–72.
[17] Park, J. K., and Kim, K. W., 2004, "Stability Analyses and Experiments of Spindle System Using New Type of Slot-Restricted Gas Journal Bearings," Tribol. Int., **37**, pp. 451–462.
[18] Huang, H., Meng, G., and Chen, J., 2007, "Investigations of Slip Effects on the Performance of Micro Gas Bearings and Stability of Micro Rotor-Bearing Systems," Sensors, **7**, pp. 1399–1414.
[19] Pan, C. H. T., 1965. "Spectral Analysis of Gas Bearing Systems for Stability Studies," *Developments in Mechanics*, Proceedings of the Ninth Midwestern Mechanics Conference, T. C. Huang and M. W. Johnson, Jr., eds., Wiley, Madison, WI, Vol. 3, pp. 431–447.
[20] Pan, C. H. T., and Kim, D., 2007, "Stability Characteristics of a Rigid Rotor Supported by a Gas-Lubricated Spiral-Groove Conical Bearing," ASME J. Tribol., **129**, pp. 375–383.
[21] Chu, L.-M., Li, W.-L., Shen, R.-W., and Tsai, T.-I., 2009, "Dynamic Characteristics of Grooved Air Bearings in Micro Systems," Proc. Inst. Mech. Eng., Part J: J. Eng. Tribol., **222**(2), pp. 109–120.